RSC Applied Interfaces

ROYAL SOCIETY OF CHEMISTRY

PAPER

View Article Online
View Journal | View Issue

Cite this: *RSC Appl. Interfaces*, 2025, **2**, 1331

Interfacial response of Mg–Ca–Si–Zr nanoparticles for transformative orthopedic therapeutics

Priya Singh,[a] Somesh Agrawal,[b] Deepak Khare,[a] Vinod Tiwari[b] and Ashutosh Kumar Dubey *[a]

Received 19th February 2025,
Accepted 26th May 2025

DOI: 10.1039/d5lf00045a

rsc.li/RSCApplInter

Debris particles, discharged due to degradation and wear, initiate an inflammatory response at the implantation site or lead to aseptic loosening of the prosthesis, ultimately resulting in implant failure over time. The toxicity concern becomes more severe with the release of nano-sized debris particles due to augmented interfacial interactions, even if the bulk counterpart is highly biocompatible. From this perspective, the present study aims to assess the *in vivo* toxicity, both local and systemic, of $Mg_{1-x}Ca_xSi_{1-x}$-Zr_xO_3 (x = 0–0.4) [MCSZO-*X*, *X* = 0–4] nanoparticles using a rat model. Initially, the *in vitro* cytotoxicity of varying concentrations (0.25, 2.5, and 25 mg ml^{-1}) of MCSZO-*X* nanoparticles was evaluated using MG-63 cells. Cell proliferation increases after the early interfacial interactions. Following this, 100 μl of MCSZO nanoparticles (25 mg ml^{-1}) was administered through intra-articular injection into the knee joint of male Wistar rats. Biochemical analyses revealed no pathological changes in the liver and kidney of the injected group of rats. Additionally, the histopathological analyses demonstrated that there is no inflammation resulting from interfacial interactions with injected nanoparticles in various organs such as the liver, heart, kidney and knee. Overall, these findings pave the way for further advancement in bone repair and implant design.

1. Introduction

The wear resistance of implants and the biological response of debris particles are key factors in determining the long-term success of implants.[1] Debris particles, released due to degradation, friction, and wear can trigger harmful biological reactions at implantation sites through interfacial interactions, resulting in periprosthetic osteolysis, inflammation, and aseptic loosening.[1,2] Specifically, inflammation activates osteoclast cells, leading to an improper balance between osteoclasts and osteoblasts. This imbalance initiates osteolysis, ultimately causing aseptic loosening of the prosthetic implant.[1–3] Additionally, the properties of debris particles, including their composition, morphology, volume, and size, play a crucial role in their biological response and profoundly affect the fate of peri-implant cells.[4]

Numerous studies (both, *in vitro* and *in vivo*) have demonstrated that nanoparticles consistently raise interfacial concerns because of their specific features such as surface area, morphology, size and concentration.[5,6] Wear particles, smaller than 2 μm, can easily enter other organs, penetrate inside the cell through the plasma membrane and induce toxicity, even at the sub-cellular level.[7,8] Wang *et al.*[8] revealed that intra-articular injection (with concentrations of 2 and 20 mg ml^{-1}) of TiO_2 nanoparticles (38 to 54 nm) into the knees of rats allowed the migration of TiO_2 nanoparticles into crucial organs like the heart and liver and resulted in pathological damage to these organs. Additionally, biochemical assessments demonstrated impairments in the renal and hepatic systems of rats.[8] Mabrouk *et al.*[9] reported that the performance of the liver is not affected after implantation of pure and BaO (3% and 5%)-doped $MgSiO_3$ nanopowders into the tibia of fractured rats.

Several studies have reported the excellent osteogenic activity and antibacterial efficiency of Mg and Ca silicate-based bioceramics *in vitro*, which substantiate the potentiality of these materials for bone tissue engineering applications.[10–17] $Mg_{1-x}Ca_xSi_{1-x}Zr_xO_3$ (x = 0–0.4) has been established as an excellent biomaterial; however, the toxicity of such nanoparticles due to interfacial interactions has not been explored. As a step ahead, this study examined the *in vivo* toxicity of $Mg_{1-x}Ca_xSi_{1-x}Zr_xO_3$ (x = 0–0.4) [MCSZO-*X* (*X* = 0–4)] nanoparticles using a rat model.

Initially, the MG-63 cells were exposed to different concentrations of MCSZO-*X* eluates (0.25, 2.5, and 25 mg ml^{-1} in normal saline) for 1 and 3 days. Following the *in vitro*

[a] *Department of Ceramic Engineering, Indian Institute of Technology (BHU), Varanasi - 221005, India. E-mail: akdubey.cer@iitbhu.ac.in; Tel: +918726823415*
[b] *Department of Pharmaceutical Engineering and Technology, Indian Institute of Technology (BHU), Varanasi, 221005, India*

results, the highest concentration (25 mg ml^{-1}) of the MCSZO-*X* nanoparticle eluates was injected into the knee joints of rats for 7 days. After the designated exposure period, the rats were euthanized. Hematological evaluations were conducted to measure white blood cell (WBC) counts and mean corpuscular volume (MCV). Additionally, biochemical analyses were performed on the serum to assess the overall functional status of the organs in the groups treated with nanoparticles, including evaluations of alkaline phosphatase and creatinine activity. The histopathological evaluations were conducted to identify any potential signs of inflammation in the major organs (kidney, heart and liver) and knee joint.

2. *In vivo* toxicity assessment of MCSZO-*X* (*X* = 0–4) nanoparticles

2.1. Sample preparation and material characterization

The procedure for synthesizing micron-sized MCSZO-*X* (*X* = 0–4) powders has been reported in our earlier work.[18] The solid-state method was employed to prepare these powders within a compositional range from *X* = 0 to *X* = 4. The particle size of the prepared micron-sized powders was reduced *via* ball milling (Fritsch Pulverisette 5) for 12–14 h at 300 rpm. For this purpose, cylindrical zirconia balls (6 mm diameter, 6 mm height, 0.9 g per ball) were used for grinding. The ratio of the balls to powder was 10 : 1. In a ball mill jar, 50 g (about 56 balls) of zirconia balls were combined with 5 g of MCSZO-*X* (*X* = 0–4) powder in 50 ml of ethanol.

2.1.1. Phase and morphological characterization. The phase verification of MCSZO-*X* nanoparticles was done *via* X-ray diffraction with Cu Kα radiation (XRD, X-ray Diffractometer, Rigaku Miniflex II Desktop) with a wavelength of 1.5418 Å (scan range: 20° to 60° and step size: 0.02°). High-resolution scanning electron microscopy (Nova Nano SEM, FEI) was used to determine the particle size and morphology of the ball-milled MCSZO-*X* nanoparticles.

2.1.2. Eluate solution preparation. The MCSZO-*X* ball-milled particles were autoclaved at 121 °C for 25–30 min. Subsequently, the sterilized powders were dispersed in normal saline (0.9% w/v NaCl) at three different concentrations: 0.25 (C1), 2.5 (C2), and 25 (C3) mg ml^{-1}. Saline served as the medium for injecting MCSZO-*X* nanoparticles into rats. To achieve uniformity in dispersed nanoparticles, the eluates were ultrasonicated for 15 min after every 6 h, over a period of 2–4 days. Before the injection, the eluates were again sterilized.

2.1.3. Leaching behavior. The leaching behavior of ready eluates (C1, C2 and C3) of MCSZO-*X* nanoparticles was examined in saline after 1, 3 and 5 days of incubation. ICP-AES was used to evaluate the amounts of leached ions (Mg, Ca, Si and Zr) from different elutes of the MCSZO-*X* samples. Before measurements, the resulting solutions were diluted 10 times with distilled water, followed by filtration using a pore size of 0.22 micron syringe filter.

2.1.4. Cellular response. The cellular behavior of MCSZO-*X* (*X* = 0–4) nanoparticles due to interfacial interactions was studied using MG-63 cells. The procured cells were grown in a CO_2 incubator under specific conditions of 37 °C temperature, 5% CO_2, and 95% humidity. The DMEM (Himedia) with 15% FBS (Gibco) and 1% antibiotic (Antibiotic-Antimycotic, Gibco) solution was used as the growth media. After 90–95% confluency, the cells were trypsinized using a 0.25% trypsin (Gibco) solution, and 10^4 cells per ml were seeded onto glass coverslips (gelatin-coated) in 24-well. The well plate was then incubated for a period of 12 h for the adhesion of cells to the substrate. After 12 h of the incubation period, 100 μl of eluates (C1, C2, and C3) of M1 M2, M3, M4 and M5 samples were added to the adhered cells. The cells with nanoparticles were further incubated for 1 and 3 days, respectively, to quantify the viability of cells. The proliferation of cells, grown on MCSZO-*X* samples, was measured using the MTT assay (3-(4,5-dimethylthiazol-2-yl)-2,5-diphenyl-tetrazolium-bromide, SRL). After cell seeding for 1 and 3 days, 500 μL of MTT reagent was added to samples. After 6 h of incubation in the prescribed environment, the well plate was removed, and the solution was replaced with DMSO (500 μL, Himedia) to dissolve the formazan crystals. After that, the culture for each sample was transferred to a 96-well plate, and the optical density was measured using an ELISA reader at a wavelength of 595 nm.

2.2. *In vivo* assessment

2.2.1. Animals. In this study, male Wister rats, weighing 250 ± 50 g, were used. Rats were housed under controlled conditions of humidity and temperature (21–25 °C ± 2 °C) with a light–dark cycle. The rats were randomly allocated to different experimental groups (*n* = 5/group). The animal experimentation protocols were authorized by the Institute Animal Ethics Committee at the Indian Institute of Technology, Banaras Hindu University, situated in Varanasi, Uttar Pradesh, India (IAEC approval number: IIT(BHU)/IAEC/2023/II/083).

2.2.2. Experimental procedure. Rats were intra-articularly administered with 100 μl of MCSZO-*X* nanoparticles (Fig. 1), suspended in sterile saline (25 mg ml^{-1}). Animals were divided into seven groups, with *n* = 5 rats in each group. Group 1 was used as a control, and group 2 was injected with saline. The remaining five groups, designated as M1, M2, M3, M4 and M5, were treated with MCSZO-*X* nanoparticles. The animals were closely observed for any signs of physical changes during the initial 30 min, following the experimental procedures. Subsequently, they were monitored at regular intervals over the next 24 h, with particular attention given to the first 4 h. Animals were observed daily for a duration of 7 days. The body weights of all the rats were measured on days 1, 3, 5 and 7 post-injection. After 7 days, blood serum was collected through retro-orbital plexus puncture. Following this, the animals were sacrificed with a high dose of

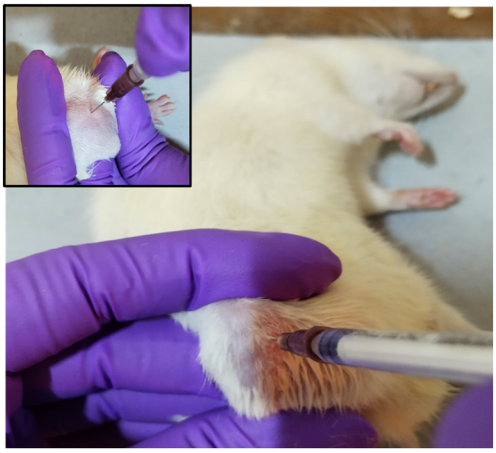

Fig. 1 Representation of the intra-articular injection of MCSZO-*X* (*X* = 0–4) nanoparticles in the Wistar rat knee (synovial) joint.

anesthesia, and the major organs (kidney, heart and liver) and knee joint were collected for histopathological studies.

2.3. Hematology and biochemical assay

The EDTA (ethylenediaminetetraacetic acid)-coated vials were used to collect the serum samples for hematological analyses, and hematologic toxicity was assessed using an automated hematological analyzer (Cell-Dyn Ruby Hematology Analyzer). Hematological parameters, such as white blood cells (WBC) and mean corpuscular volume (MCV), were estimated. Biochemical testing was performed on the serum, which was obtained after centrifugation (4000 RPM for 10 min) of blood samples, to evaluate the activities of creatinine and alkaline phosphatase (ALP) in rats injected with nanoparticles and compared with the control and saline-treated groups. AUTOSPAN liquid and MKB alkaline phosphatase kits were used for the determination of ALP activity. The entire test was conducted as per the guidelines provided by the manufacturer. Additionally, creatinine levels were also measured using a standard kit (Crystal Chem, IL, USA).

2.4. Histopathological analyses

The fixed tissues, including the kidney, liver, and heart, were dehydrated using a series of ethanol solutions. The paraffin blocks were made after fixing them with paraffin wax. Hematoxylin and eosin (H & E) stains were used for staining the tissue blocks after they were divided (10 μm) for histopathological evaluations. The tissues of the fixed knee joint were first dehydrated with ethanol solution, and then decalcification was done with nitric acid solution (10%). The paraffin-embedded joint tissue blocks were prepared for histopathological examination, following a similar procedure to other organs. Nikon Eclipse LV 100 ND fluorescence microscope photographs of stained tissues were obtained.

2.5. Statistical analyses

The SPSS software was used to investigate statistically significant differences among various tests using the one-way ANOVA method and Tukey's *post hoc* tests, at a $p \leq 0.05$. For *in vivo* data analyses, Graph Pad Prism software was used. The body weights of animals were statistically examined through the application of two-way ANOVA, whereas the hematological parameters were assessed *via* one-way ANOVA (at $p > 0.05$).

3. Results and discussion

3.1. Phase analyses

Fig. 2 represents the XRD patterns of MCSZO-*X* (*X* = 0–4) nanoparticles. The XRD pattern confirms the formation of a monoclinic pure $MgSiO_3$ [JCPDS # 35-0610] phase with the *P*21/*c* space group. In addition, a few minor peaks were indexed with JCPDS # 34-0189 using the *Pmnb* space group. However, the peak shifted towards a lower angle with the

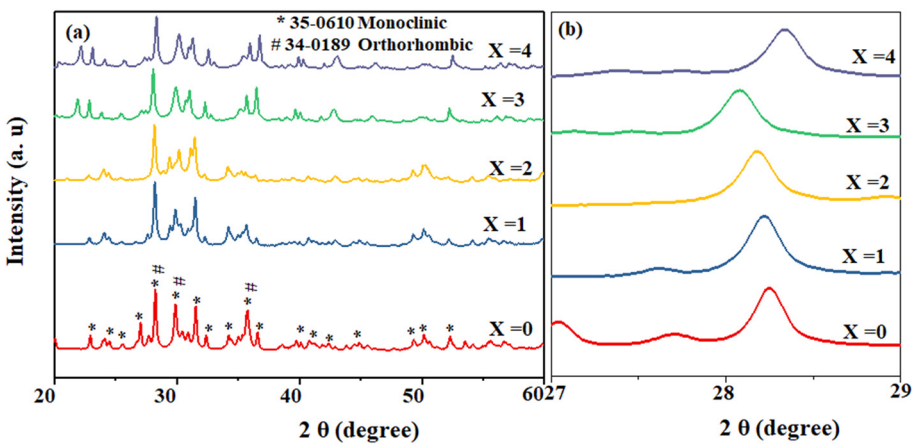

Fig. 2 XRD results of MCSZO-*X* (*X* = 0–4) nanoparticles. (a) XRD patterns of different samples of MCSZO (*X* = 0–4), calcined at 1300 °C for 10 h. (b) Enlarged view of the highest intense peaks of samples.

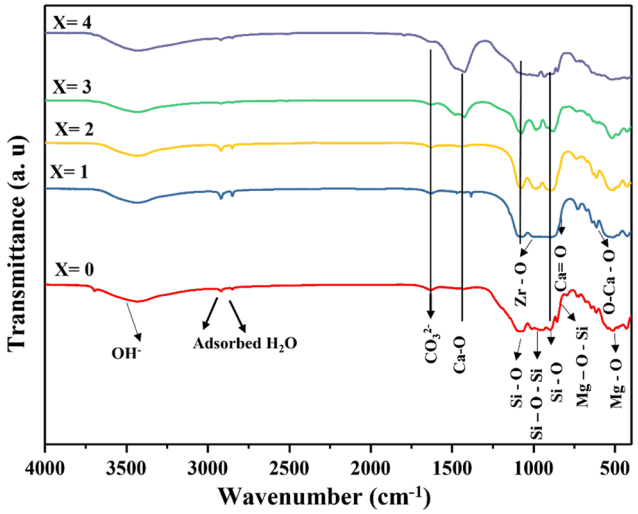

Fig. 3 FT-IR spectra of MCSZO-*X* (*X* = 0–4) nanoparticles.

incorporation of Ca/Zr, increasing the concentration from *X* = 0 to *X* = 3, as shown in Fig. 2b. Moreover, the crystallite size was calculated using Scherrer's formula.[19,20] The crystallite size decreased from 35 nm to 31 nm as the Ca/Zr increased from *X* = 0 to *X* = 3. After that, the crystallite size again increases from 31 nm to 33 nm with an increase in the amount of Ca/Zr, from *X* = 3 to *X* = 4.

Fig. 2b demonstrates that with increasing concentration from *X* = 0 to *X* = 3, the peaks shift towards lower 2θ values from 28.24° to 28.08°. With a further increase in concentration from *X* = 0 to *X* = 3, the peak shifts towards the higher angle again from 28.08° to 28.33° (as represented by the enlarged view). The incorporation of larger Ca^{2+} cations (1.34 Å) at the reduced Mg^{2+} site (0.72 Å) and Zr^{4+} cations (0.74 Å) at the diminutive Si^{4+} site (0.40 Å) leads to an expansion of the lattice in $MgSiO_3$ as the concentrations of Ca and Zr increase from 0 to 0.3, resulting in peak shifts toward lower 2θ values. Nonetheless, as the concentration increases beyond 0.3, the peaks shift to higher angles owing to lattice contraction, stemming from the presence of a greater quantity of Ca^{2+} at the Mg^{2+} site.[11,21–23]

The five polymorphic variants of $MgSiO_3$ adopt either monoclinic or orthorhombic crystal structures.[24] As the concentration of Ca and Zr increased from 0 to 0.2, peak positions in the X-ray diffraction patterns shifted to lower 2θ angles, from 22.96° to 22.82°. This shift results from the substitution of larger Ca^{2+} ions for smaller Mg^{2+} ions at the A-site and Zr^{4+} ions for smaller Si^{4+} ions at the B-site. Conversely, increasing the Ca and Zr concentrations from 0.2 to 0.4 caused the peaks to shift to higher 2θ values, from 22.82° to 23.12°, likely due to lattice contraction in MCSZO-*X* bioceramics driven by greater Ca^{2+} substitution at the Mg^{2+} sites. For compositions with *x* = 0.3 to *x* = 0.4, phase analyses revealed minor secondary phases, ZrO_2 (JCPDS # 37-1484), $CaSiO_3$ (JCPDS # 43-1460) and $CaMgSiO_4$ (JCPDS # 19-0240). The emergence of an additional secondary phase, Mg_2SiO_3, poses challenges in synthesizing single-phase $MgSiO_3$. Therefore, with increasing Ca and Zr concentrations from 0.3 to 0.4, further minor phases, including ZrO_2, $CaSiO_3$, Ca_2MgSiO_7, Mg_2SiO_4, and $CaMg(SiO_3)_2$, began to appear.

The FT-IR spectra of MCSZO-X nanoparticles confirmed the incorporation of Ca/Zr in the $MgSiO_3$ structure (Fig. 3). The specific peaks of Si–O at 470, 500, 600, and 1052 cm^{-1} correspond to bending and stretching vibrations, respectively. The bending vibration observed at around 800 cm^{-1} in Si–O–Si indicates the formation of $MgSiO_3$.[25,26] Moreover, the vibrational peak, representing Si–O within silicate tetrahedra, is observed at 682 cm^{-1}.

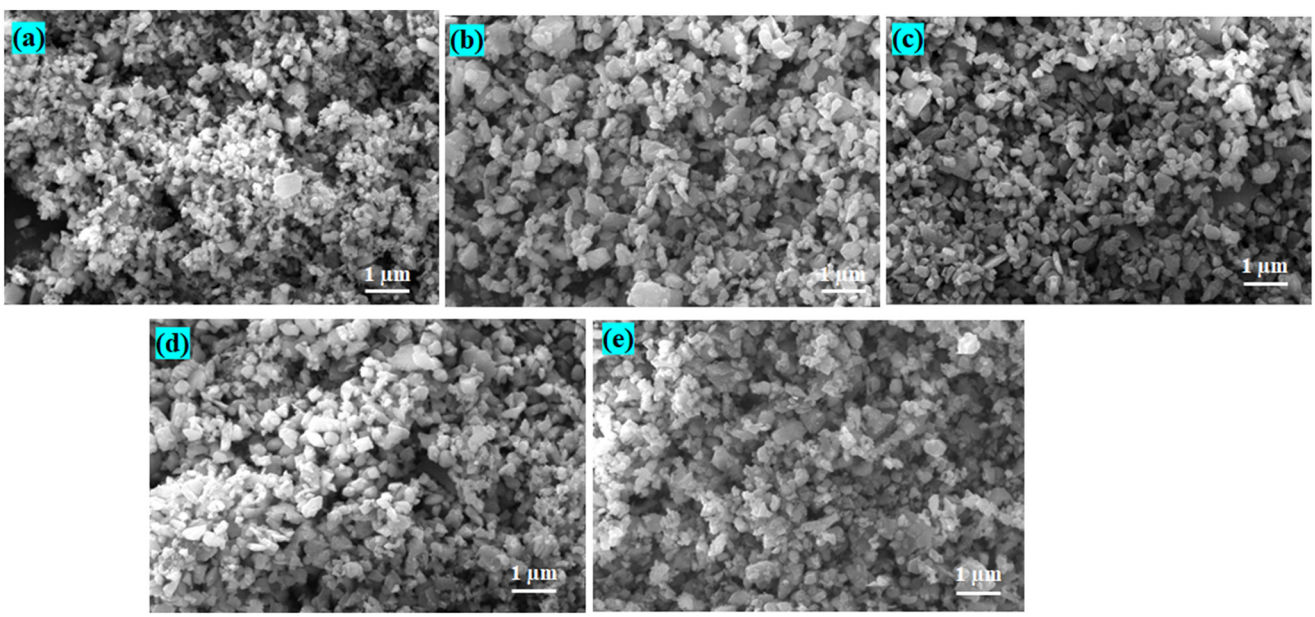

Fig. 4 Scanning electron micrographs of MCSZO-*X* nanoparticles. (a) *X* = 0, (b) *X* = 1, (c) *X* = 2, (d) *X* = 3 and (e) *X* = 4.

Furthermore, the stretching and bending vibrations of Mg–O are associated with the vibrational bands at 517 cm^{-1} and a peak close to 870 cm^{-1}.[27] Additionally, the peaks at 1320 cm^{-1} and 1127 cm^{-1} correspond to the stretching vibrations of C═O and C–O, respectively.[28]

3.2. Microstructural analyses

Fig. 4 represents the high-resolution scanning electron microscopic (HRSEM) images of MCSZO-*X* nanoparticles. The average particle size of MCSZO-*X* nanoparticles increased from 346 to 452 nm as the amount of Ca/Zr in MCSZO-*X* was raised from 0 to 4.

3.3. Leaching behavior

Fig. 5 illustrates the amounts of Ca^{2+}, Mg^{2+}, Si^{4+}, and Zr^{4+} ions, leached from the MCSZO-*X* nanoparticles after 3, 5, and 7 days of immersion in saline. The leaching of Mg^{2+} and Si^{4+} ions from different nanoparticles (M1, M2, M3, M4, and M5) are lower in comparison to pure MCSZO-*X* (*X* = 0) nanoparticles as the concentration of Mg^{2+} and Si^{4+} decreases with increasing concentrations of Ca^{2+} and Zr^{4+} dopants. However, the leaching of Ca^{2+} and Zr^{4+} ions increases. In addition, the amount of Ca^{2+} leached from MCSZO-*X* nanoparticles also increased with an increase in the immersion time.

Bones incorporate ions such as Mg^{2+}, Ca^{2+}, Zr^{4+}, and Si^{4+}, which play vital roles in regulating various metabolic activities, including supporting bone formation and reducing the risk of osteoporosis.[10,29–32] Ca plays a vital role and also affects the metabolic functions of osteoblast cells.[29,33] Concentrations of Ca^{2+} ions, above 10 mM, have been shown to exert cytotoxic effects, whereas levels in the 2–4 mM range support osteoblast proliferation and differentiation, thereby, enhancing the osteogenic response.[34] Si is essential for bone development and overall bone health.[10] Incorporating zirconium into Ca–Si-based bioceramics, like baghdadite, has been reported to enhance the attachment and growth of osteoblast-like cells.[35]

3.4. Cell viability

The viability of MG-63 cells was evaluated using the MTT assay at different elute concentrations (C1, C2, and C3 for M1, M2, M3, M4 and M5 samples). Fig. 6 demonstrates the proliferation of MG-63 cells on the prepared MCSZO-*X* nanoparticles after 1 and 3 days of incubation. The viability of osteoblast-like MG-63 cells, cultured on MCSZO-*X* nanoparticles, was lower than that of the control after 1 day.

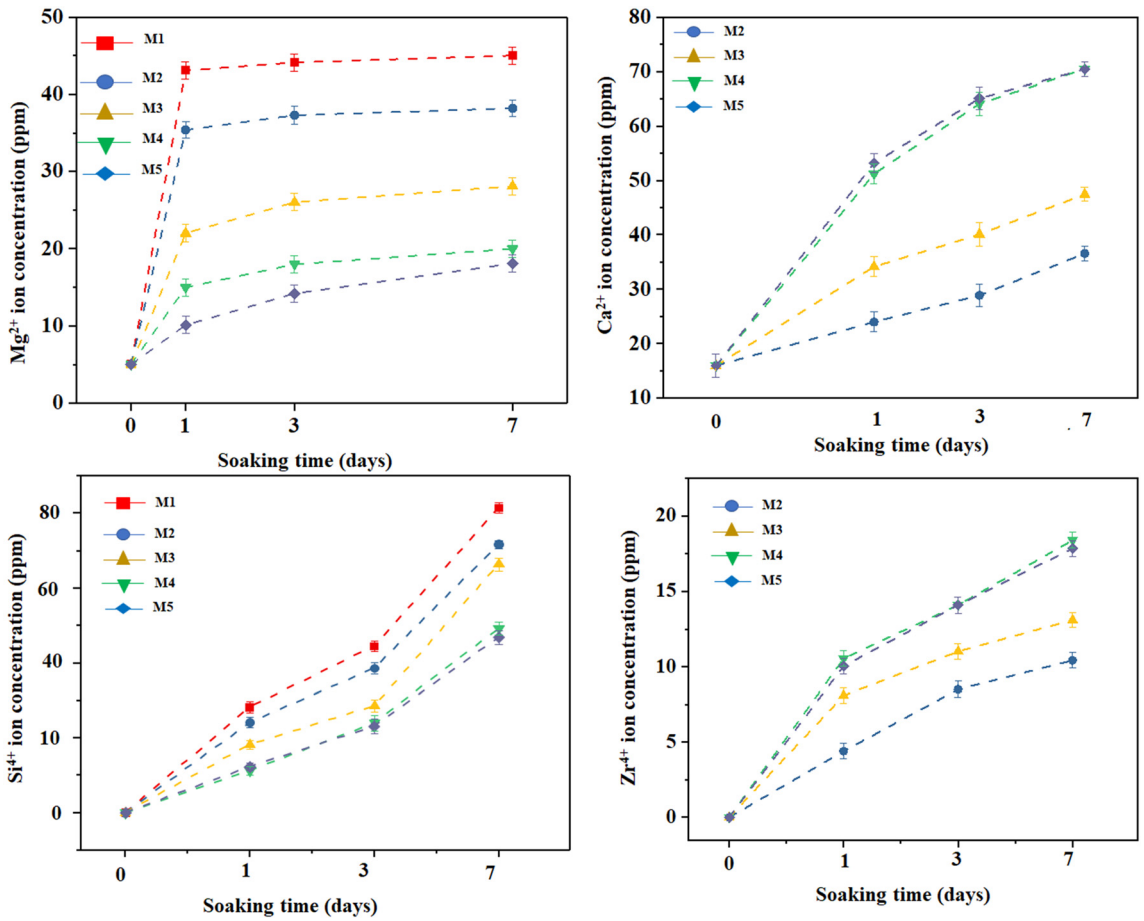

Fig. 5 Leaching behavior of Mg^{2+}, Si^{4+}, Ca^{2+}, and Zr^{4+} ions from MCSZO-*X* nanoparticles in saline.

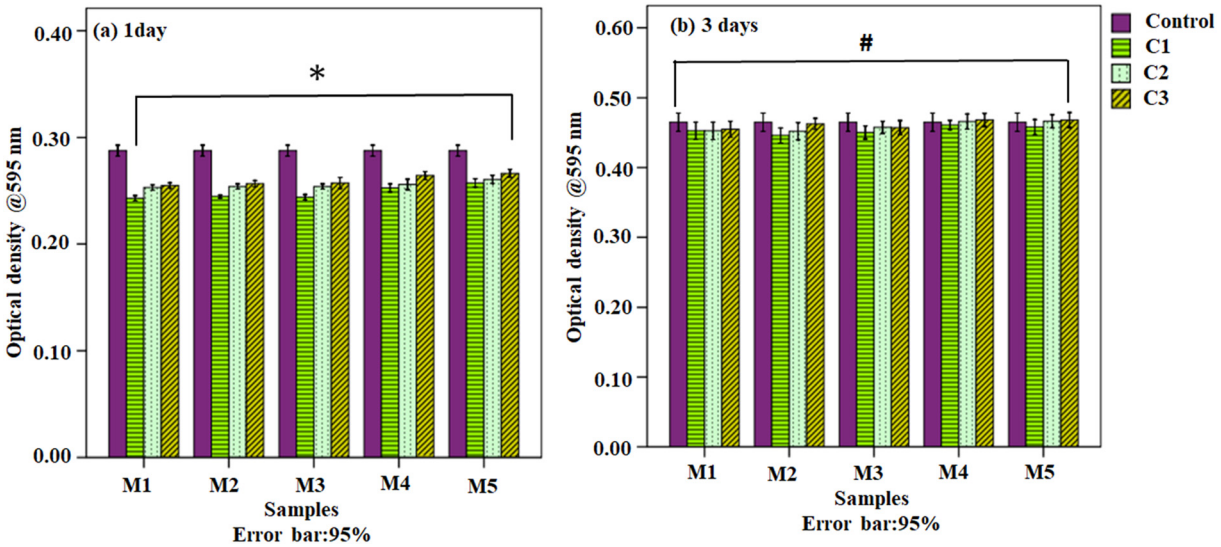

Fig. 6 Optical density of MG-63 cells after 1 and 3 days of culture on MCSZO-*X* (*X* = 0–4); [(M1, M2, M3, M4 and M5) nanoparticles at different concentrations, *i.e.*, 0.25, 2.5 and 25 mg ml^{-1} samples] and HA, used as a control. The asterisk symbol (*) indicates the significant variation in optical density across all MCSZO-*X* samples (M1, M2, M3, M4 and M5) at different concentrations, compared to the control after 1 day of culture as [Fig. 6(a)]. However, symbol (#) shows significant variation in optical density across all MCSZO-*X* (M1, M2, M3, M4 and M5) nanoparticles, cultured for 3 days compared to the entire MCSZO-*X* samples, cultured for 1 day [Fig. 6(b)].

This is probably due to the physical damage of the cells resulting from early-stage interaction with nanoparticle eluates. Notably, the viability of cells was significantly improved across all concentrations of MCSZO-*X* nanoparticles after 3 days of culture in comparison to the results obtained after 1 day of incubation. For these samples, the viability was comparable to that of the control group [Fig. 6(b)].

3.5. *In vivo* studies

3.5.1. General observation. After injecting the MCSZO-*X* particles for seven days, the skin texture and salivation of the rat remained unchanged. Also, after the intra-articular injection, the rats did not exhibit symptoms such as diarrhea, tremor, or convulsions. Additionally, after seven days of post-injection, no notable changes were observed in the behavior of rats. Also, the injection sites in the different rat groups did not display any signs of inflammation (swelling or redness) throughout the observation period. Digital cameras were used to take paw photographs of the rats, *i.e.*, the group injected with MCSZO-*X* particles, which were then compared to the paw images of the control and saline-treated groups [Fig. 7].

The paws of the rats, injected with MCSZO-*X* nanoparticles (M1, M2, M3, M4 and M5), are similar to those of the saline-treated and control rats, revealing no indication of abnormalities, inflammation, redness, or edema. Likewise, after completion of the experiment, the knee joints of the control, saline and treated rats displayed unchanged morphology.

Furthermore, as aforementioned, no inflammation was detected at the injection site, and no signs of atrophy were noted in the adjacent bone structures, such as the tibia and femur. This result corresponds to the *in vitro* cytocompatibility of MCSZO-*X* nanoparticles with varying concentrations of Ca/Zr [Fig. 6].

3.5.1.1. Impact of intra-articular injection of MCSZO-X on body weight. The variation in body weight is crucial for assessing whether the injected nanoparticles have adversely affected the function of vital organs.[36,37] Consequently, before and after (after 7 days) the injection, the weights of each of the 35 rats were recorded. The control, saline, and MCSZO-*X* nanoparticle-injected rats did not show any significant weight changes [Fig. 8]. Statistical analyses using two-way ANOVA showed no noticeable variation in body weight.[38]

3.5.2. Hematological analyses. Changes in hematological parameters in humans and animals are indicative of drug-induced toxicity. The hematopoietic system is a vital body system that produces the cellular components of blood.[38] In this study, the effects of intra-articularly injected MCSZO-*X* nanoparticles on the blood cells, such as WBC and MCV, were evaluated as compared to the control group [Fig. 9]. The evaluation of basic hematological parameters, such as the measurements of WBC and MCV, is a crucial stage in the toxicity detection process.

The statistical analyses revealed no significant variation in WBC ($p > 0.05$) among all groups in the MCSZO-*X* nanoparticle-injected rats in comparison to the saline group [Fig. 9(a)]. Also, there were no notable changes in the MCV ($p > 0.05$) among all the injected MCSZO-*X* nanoparticle groups as compared to the saline groups [Fig. 9(b)].

3.5.3. Biochemical assays. The impact of MCSZO-*X* nanoparticles (*X* = 0–4) on enzyme levels in rat blood was

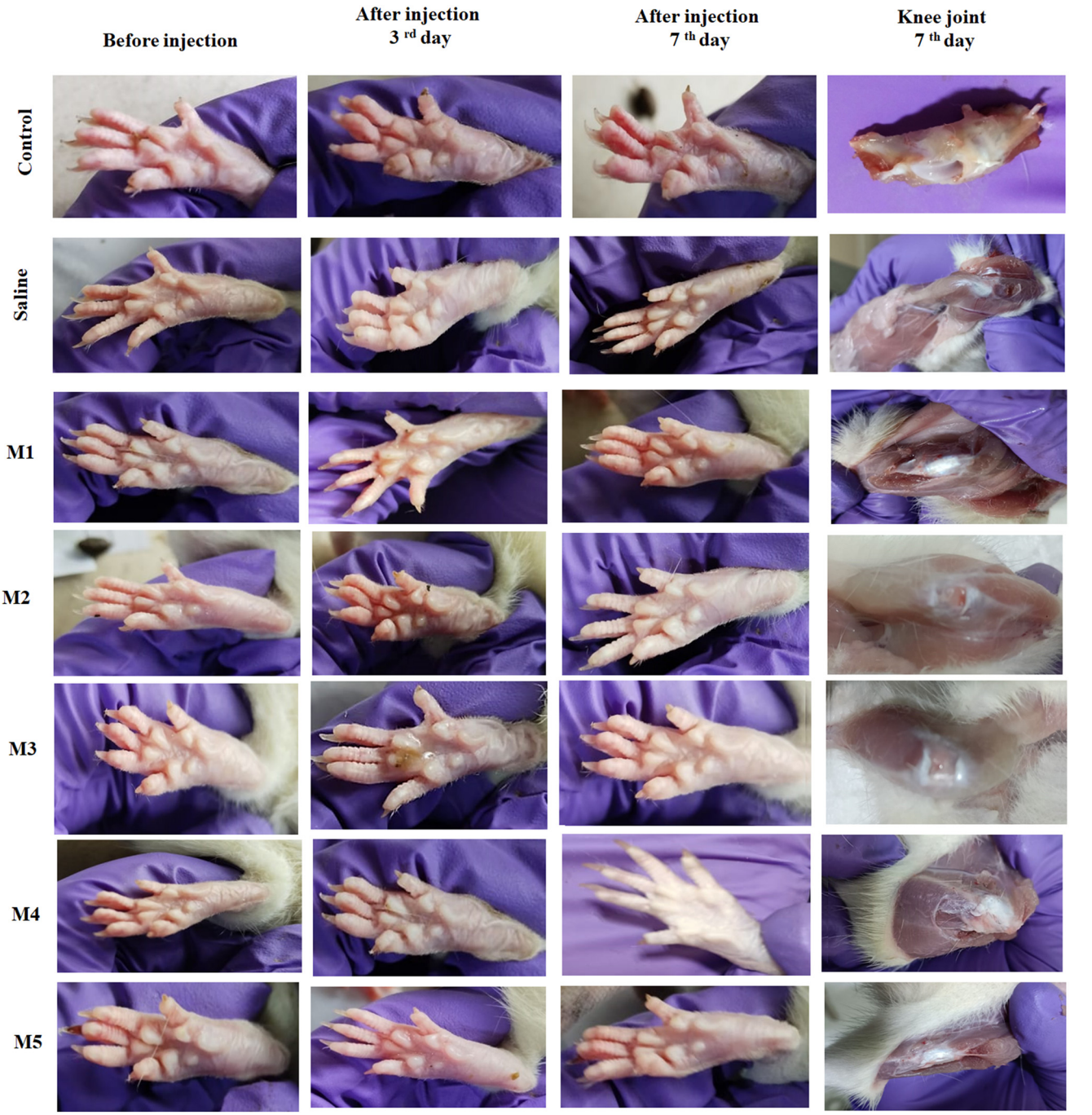

Fig. 7 Digital camera images of rat paws before injection and on the 3rd and 7th day after receiving injections of MCSZO-*X* nanoparticles into their knee joints along with the knee joint images (after 7th day).

assessed by analyzing the biochemical properties of the extracted serum.

Typically, the hepatic function is assessed by measuring the serum ALP activity level. The breakdown and restoration of liver tissue contribute to alterations in ALP activity.[39,40] Additionally, hepatotoxicity raised by chemicals or drugs also increases the ALP activity in blood serum.[41,42]

As a result, the liver is an essential organ for examining the impact of toxicity induced by nanoparticles. In this study, MCSZO-*X* nanoparticles were injected into the synovial joint.

ALP, a marker of bone formation, plays a crucial role in determining whether exposure to MCSZO-*X* nanoparticles leads to any bone abnormalities. The statistical analyses reveal that there were no significant changes in the serum levels (ALP) between the control and MCSZO-*X* nanoparticle-treated (M1, M2, M3, M4 and M5) groups [Fig. 10(a)]. Consequently, exposure to MCSZO-*X* nanoparticles did not

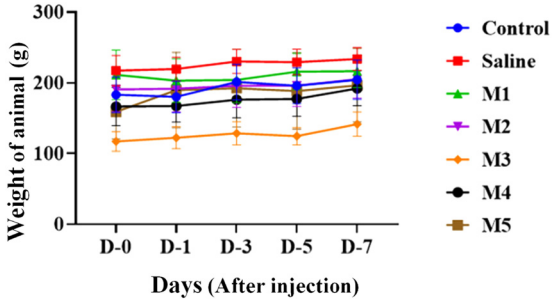

Fig. 8 Effect of intra-articular injection of MCSZO-*X* (M1, M2, M3, M4 and M5) nanoparticles on the body weight of rats throughout the experiment. All results are shown as mean ± standard deviation (*n* = 5 per group).

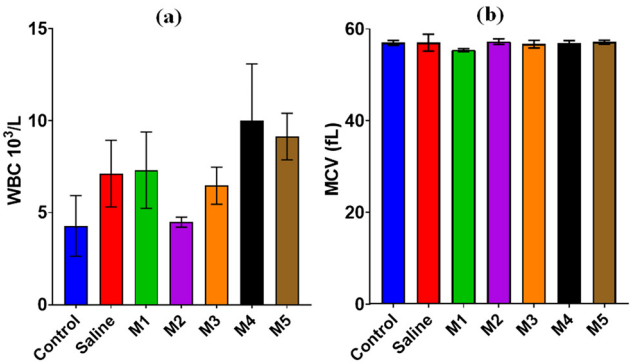

Fig. 9 Effect of intra-articular injection of MCSZO-*X* nanoparticles in rats. (a) WBC count and (b) MCV on day 7 of injection. All results are shown as mean ± standard deviation (*n* = 5 per group).

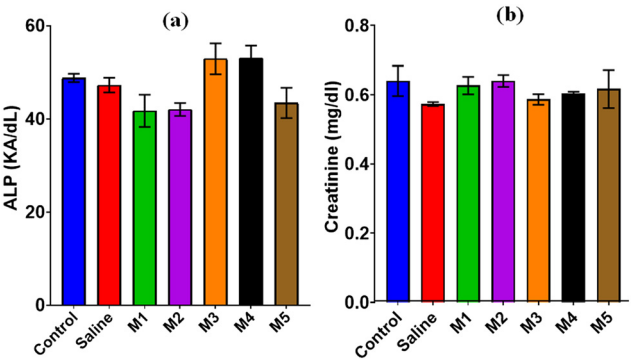

Fig. 10 Effect of MCSZO-*X* nanoparticles on serum concentration after 7 days of post-injection in rats. (a) ALP and (b) creatinine level. All results are shown as mean ± standard deviation (*n* = 5 per group).

alter the liver function. Moreover, assessing serum creatinine levels is a typical method for detecting potential adverse effects on renal function caused by the implant or foreign particles.[43]

Elevated blood creatinine levels indicate reduced kidney filtration capacity.[44–47] In this study, the creatinine levels in the blood serum of rats, injected with M1, M2, M3, M4 and M5 nanoparticles, do not show any substantial differences compared to the saline group [Fig. 10(b)]. Also, the MCSZO-*X* nanoparticles did not cause kidney impairment.

3.5.4. Histopathological analyses. Over the period of seven days, it is possible that the nanoparticles, injected into the intraarticular region, can enter the bloodstream and reach organs like the liver, kidney, lungs and heart as a result of regular physiological processes. Therefore, histopathological analyses of the liver, heart, kidney and knee were performed to determine the toxicity of MCSZO-*X* (*X* = 0–4) nanoparticles. The comparison of histological images of various stained organs from particulate-injected groups (M1, M2, M3, M4, M5) with those of the control and saline-injected groups are shown in Fig. 11–14.

The sections of all the stained organs, in general, reveal a normal appearance without the presence of eluate particles. The MCSZO-X treated groups (M1, M2, M3, M4, and M5) showed no signs of tissue shrinkage, cardiac muscle disorder, vacuolization, and bleeding. The muscle fibers appear straight and organized, similar to those in the control group (Fig. 11). The connective tissues of the hearts in the nanoparticle-treated rat groups show normal architecture. In several studies, it has been observed that exposure to fine concentrated particles can result in irregular beats and, in some cases, cardiac dysfunction.[48–52] The injection of TiO_2 nanoparticles has been shown to cause swelling of the endothelial cells of the heart after 7 days.[8]

In this study, the hearts of rats in the M1, M2, M3, M4 and M5 eluate-treated groups did not exhibit enlarged endothelial cells [Fig. 11]. Overall, the cardiac tissues of the rats treated with MCSZO-*X* (M1, M2, M3, M4 and M5) reveal no histopathological changes. Evidently, the kidney is the main organ of the body that removes foreign nanoparticles.[6] As the kidney removes foreign substances from the body by filtering, it is crucial for the kidney to participate in the release of nanoparticles if they reach vital organs. Besides, the histopathology analyses of the kidney tissue are crucial for both identifying the nanoparticles and determining how they may affect the structure and functioning of the kidneys.

Exposure to different nanoparticles, such as ZnO, Au, and TiO_2, causes pathological alterations in the kidney, including necrosis, dispersed glomeruli, and tubular dilatation.[8,53–55] However, in comparison to the control rat groups, the histopathological images of the kidney sections of the rats injected with MCSZO-*X* particles (M1, M2, M3, M4 and M5) show unchanged renal tubules within the cortex (absence of any indication of vacuolar degeneration) [Fig. 12].

The kidney sections of rats, treated with the control and MCSZO-*X* groups, show normal renal cortex and glomerular cells without tubule dilation. Overall, histology of the kidney sections reveals that the intra-articularly injected MCSZO-*X* nanoparticles (M1, M2, M3, M4 and M5) have no adverse effect on the kidney.

The liver plays a main role in detoxifying the body. This means that the foreign particles can move through the circulatory or lymphatic systems and into the liver.[56–58] Cytoplasmic vacuolization disrupts the function of the

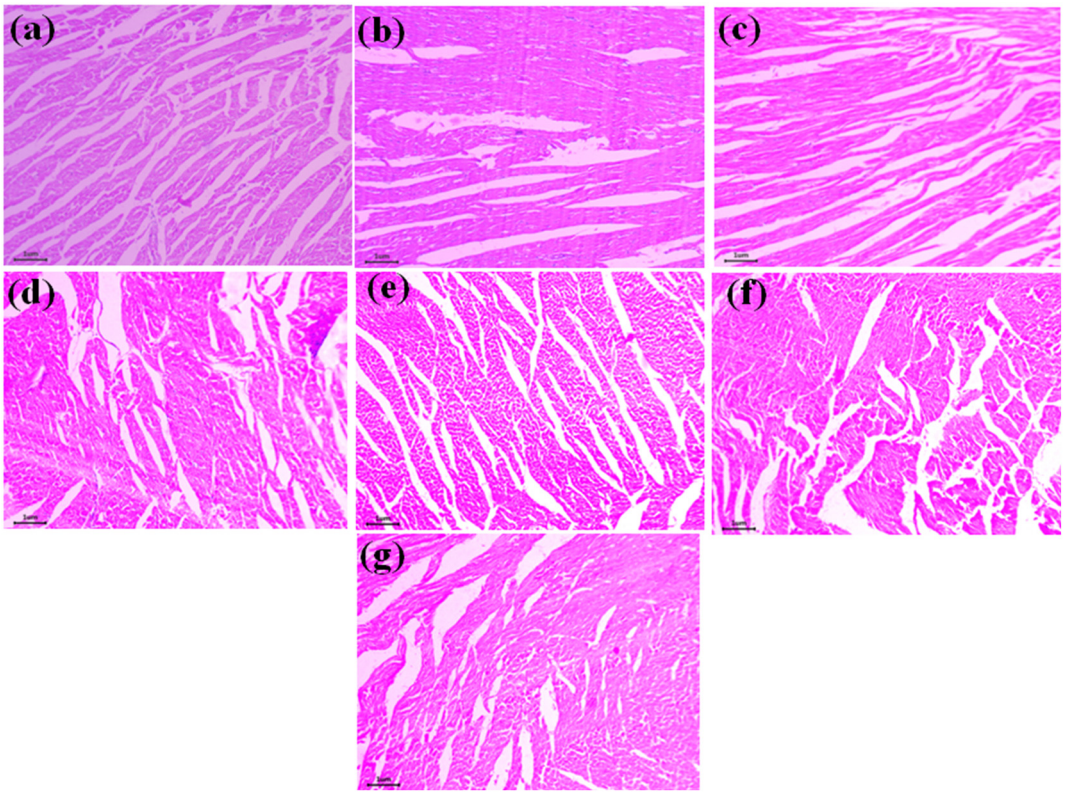

Fig. 11 Histopathological images of the heart tissues, stained with H & E, after 7 days of injection in the following groups of rats: (a) control (non-injected), (b) saline, (c) M1, (d) M2, (e) M3, (f) M4 and (g) M5 nanoparticle eluate-treated groups (scale bar: 1 μm).

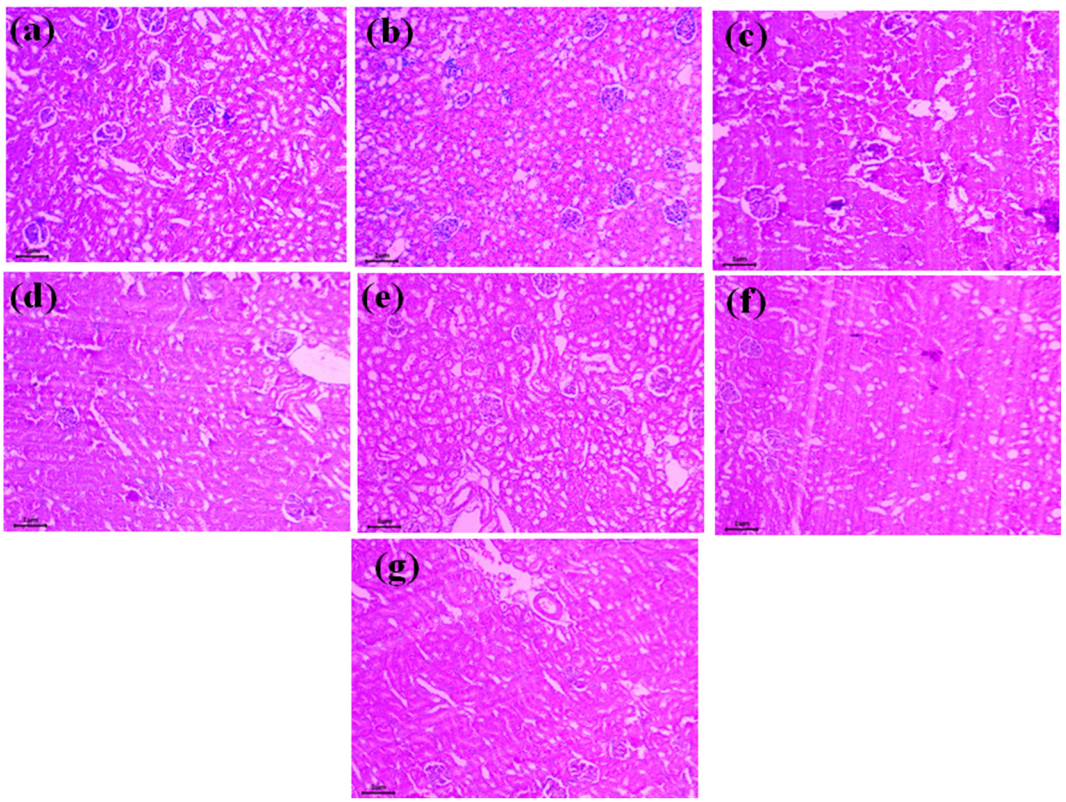

Fig. 12 Histopathological images of the kidney tissues, stained with H & E, after 7 days of injection in the following groups of rats: (a) control (non-injected), (b) saline, (c) M1, (d) M2, (e) M3, (f) M4 and (g) M5 nanoparticle eluate-treated groups (scale bar: 1 μm).

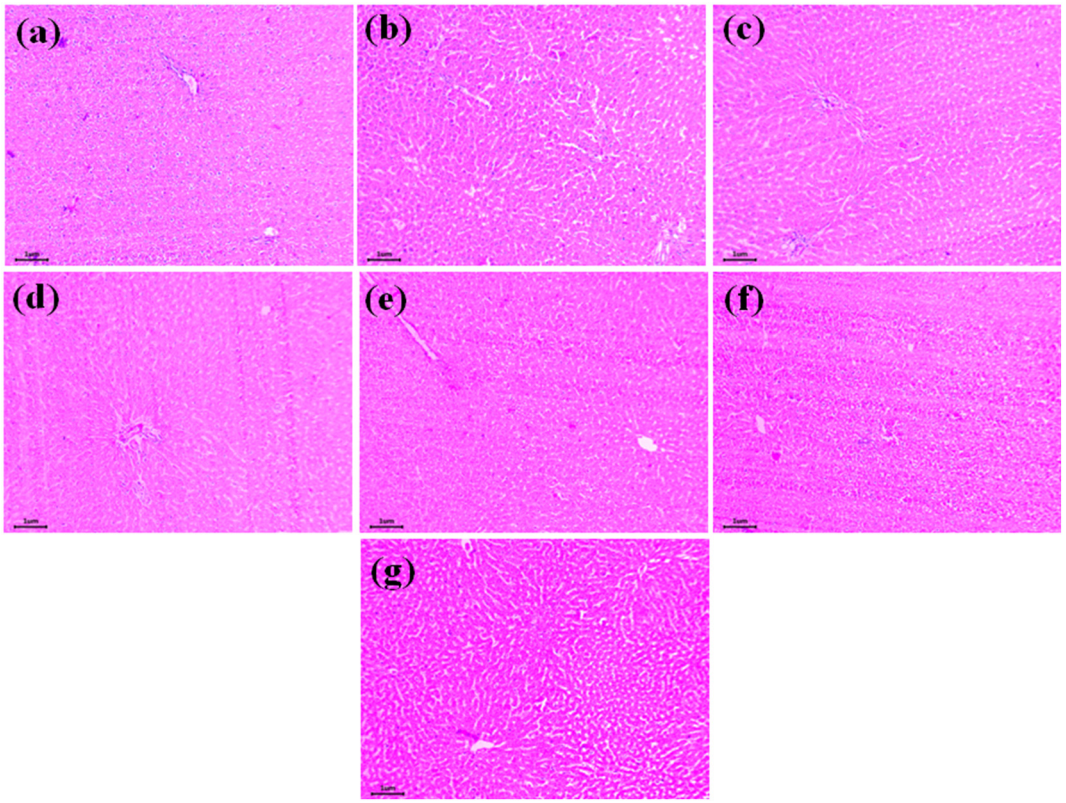

Fig. 13 Histopathological images of the liver section, stained with H & E, after 7 days of injection in the following groups of rats: (a) control (non-injected), (b) saline, (c) M1, (d) M2, (e) M3, (f) M4 and (g) M5 nanoparticle eluate- treated groups (scale bar: 1 μm).

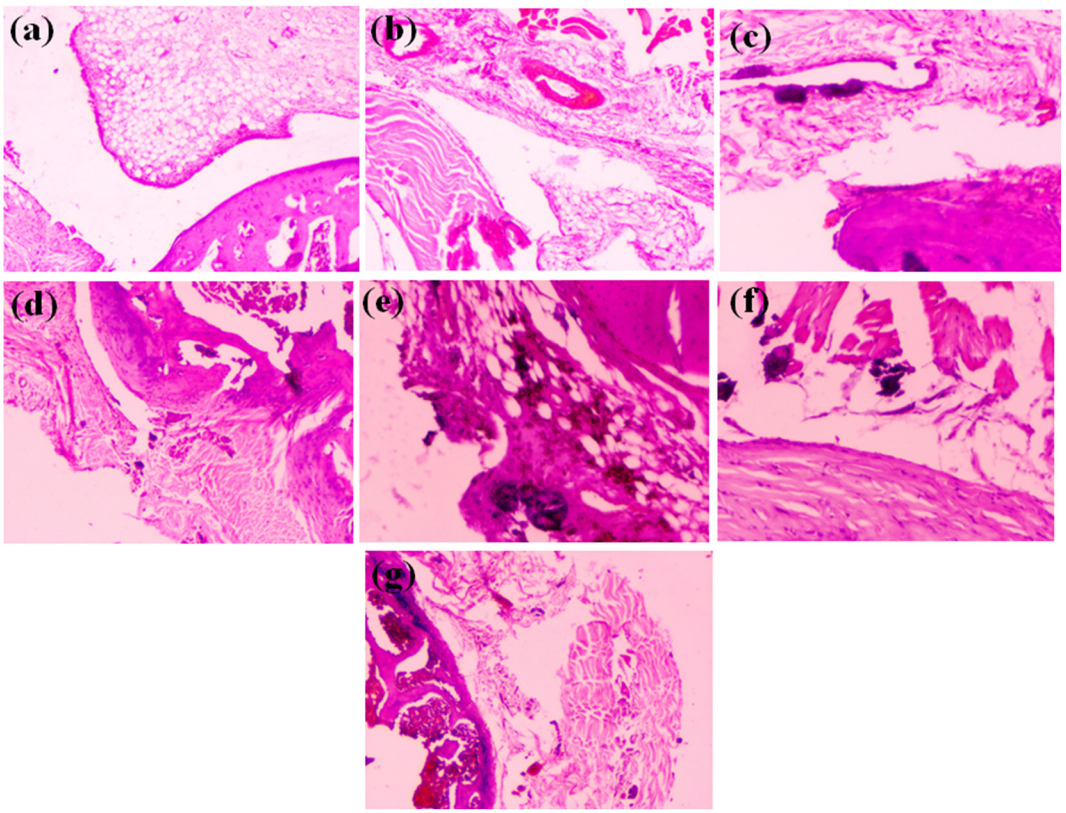

Fig. 14 Histopathological features of rat knee joint tissue, stained with H & E, after 7 days of intra-articular injection in the following groups of rats: (a) control (non-injected), (b) saline, (c) M1, (d) M2, (e) M3, (f) M4 and (g) M5 nanoparticle eluate-treated groups (scale bar: 1 μm).

membrane and can occasionally be a sign of liver injury.[59–61] In this study, there is no evidence of any vacuolization in the cytoplasm of hepatocytes in the livers of the rats, treated with MCSZO-*X* nanoparticles. As a result, histological features of liver cells injected with MCSZO-*X* particles (M1, M2, M3, M4 and M5) revealed no indications of damage, bleeding, or necrosis near the sinusoids when compared to those of control and saline rats [Fig. 13].

Overall, the histopathological images of the organs, stained with H & E of the M1, M2, M3, M4 and M5 injected nanoparticles reveal a normal appearance comparable to that of the control and saline groups. The major organs of the rats in the nanoparticle-treated groups show no evidence of particle dissemination.

The histological images provide a clear indication of the presence of nanoparticles within the fibroadipose tissue surrounding the synovial joint [Fig. 14(a–e)]. Moreover, the absence of macrophage infiltration is clearly seen [Fig. 14(c–e)], which suggests the biocompatible nature of the prepared MCSZO-*X* nanoparticles.[62,63] Furthermore, the administration of MCSZO-*X* nanoparticles *via* intra-articular injection did not lead to any injury to the cartilage or excessive growth of the synovial membrane. The thickening of the synovial membrane occurs due to an increased density of cells resulting from the influx of different cell types.[64–66] The histological analyses of the knee joint did not reveal any negative response to the intra-articular administration of MCSZO-*X* nanoparticles.

The histological analyses of rats, treated with MCSZO-*X* (M1, M2, M3, M4 and M5) nanoparticles show no signs of inflammation at the implantation site of injection (synovial joint) or in vital organs [Fig. 14]. Moreover, MCSZO-*X* nanoparticles promote the proliferation of MG-63 cells [Fig. 6]. Overall, MCSZO-*X* nanoparticles demonstrate *in vitro* cytocompatibility and *in vivo* biocompatibility.

In ceramic-based implants, the wear debris particles, such as Al_2O_3 and ZrO_2, are typically submicron in size.[67,68] Earlier studies have reported that macrophages engulf submicron-sized particles, which increases the risk of an adverse reaction or inflammation.[7,69,70] However, histological images of knee joints treated with MCSZO-*X* nanoparticles showed no signs of macrophage infiltration (Fig. 14(c–f)), suggesting that MCSZO-*X* nanoparticles are biocompatible.

4. Conclusion

In vitro investigations indicate that $Mg_{1-x}Ca_xSi_{1-x}Zr_xO_3$ nanoparticles promote the proliferation of MG-63 cells up to a concentration of 25 mg ml^{-1} after initial interfacial interactions. The *in vivo* assessment revealed that the nanoparticles, injected intraarticularly into the rats, did not migrate to any of the major organs, including the kidney, heart and liver. In addition, the non-toxicity of $Mg_{1-x}Ca_xSi_{1-x}Zr_xO_3$ nanoparticles has been established through histological analyses of the knees and vital organs of rats exposed to nanoparticle eluates at concentrations of 0.25, 2.5 and 25 mg ml^{-1}. Also, the absence of nanoparticles within the essential organs suggests that they were not transported to these organs. The histology of the knee tissues of the rats treated with nanoparticles reveals the absence of any indications of inflammation. Furthermore, biochemical parameters (ALP and creatinine) revealed that $Mg_{1-x}Ca_xSi_{1-x}Zr_xO_3$ nanoparticles had no toxic effect on the functioning of vital organs.

Data availability

The data will be made available upon request.

Conflicts of interest

The authors declare no conflicts of interest.

Acknowledgements

This research was financially supported by SERB (CRG/2022/002154), Government of India. The authors sincerely thank Dr Bitan Naik from the Department of Pathology, Institute of Medical Sciences (IMS), Banaras Hindu University (BHU), Varanasi, for histopathological imaging.

References

1 L. Zhang, E.-M. Haddouti, K. Welle, C. Burger, D. C. Wirtz and F. A. Schildberg, *et al.* The effects of biomaterial implant wear debris on osteoblasts, *Front. Cell Dev. Biol.*, 2020, **8**, 352.
2 C. Y. Hu and T.-R. Yoon, Recent updates for biomaterials used in total hip arthroplasty, *Biomater. Res.*, 2018, **22**(1), 1–12.
3 I. D. Learmonth, C. Young and C. Rorabeck, The operation of the century: total hip replacement, *Lancet*, 2007, **370**(9597), 1508–1519.
4 A. A. Stratton-Powell, K. M. Pasko, C. L. Brockett and J. L. Tipper, The biologic response to polyetheretherketone (PEEK) wear particles in total joint replacement: a systematic review, *Clin. Orthop. Relat. Res.*, 2016, **474**(11), 2394–2404.
5 Z. Chen, H. Meng, G. Xing, C. Chen, Y. Zhao and G. Jia, *et al.* Acute toxicological effects of copper nanoparticles in vivo, *Toxicol. Lett.*, 2006, **163**(2), 109–120.
6 T. Ding, Y. Xue, H. Lu, Z. Huang and J. Sun, Effect of particle size of hydroxyapatite nanoparticles on its biocompatibility, *IEEE Trans. NanoBiosci.*, 2012, **11**(4), 336–340.
7 K. J. Margevicius, T. W. Bauer, J. T. McMahon, S. A. Brown and K. Merritt, Isolation and characterization of debris in membranes around total joint prostheses, *J. Bone Jt. Surg., Am. Vol.*, 1994, **76**(11), 1664–1675.
8 J.-X. Wang, Y.-B. Fan, Y. Gao, Q.-H. Hu and T.-C. Wang, TiO2 nanoparticles translocation and potential toxicological effect in rats after intraarticular injection, *Biomaterials*, 2009, **30**(27), 4590–4600.

9 M. Mabrouk, G. Ibrahim Fouad, H. H. Beherei and D. B. Das, Barium Oxide Doped Magnesium Silicate Nanopowders for Bone Fracture Healing: Preparation, Characterization, Antibacterial and In Vivo Animal Studies, *Pharmaceutics*, 2022, **14**(8), 1582.
10 P. Singh, X. Yu, A. Kumar and A. K. Dubey, Recent advances in silicate-based crystalline bioceramics for orthopedic applications: a review, *J. Mater. Sci.*, 2022, **57**(28), 13109–13151.
11 P. Singh and A. K. Dubey, Accelerated Osteogenic Response of Electrodynamically Stimulated Mg1–xCaxSi1–xZrxO3 (x = 0–0.4) Bioelectrets, *ACS Biomater. Sci. Eng.*, 2023, **9**(11), 6293–6308.
12 P. Singh and A. K. Dubey, Electret-induced antibacterial response of Mg1-xCaxSi1-xZrxO3 (x= 0–0.4) bioceramics, *J. Am. Ceram. Soc.*, 2024, **107**(6), 4263–4281.
13 S. K. Venkatraman and S. Swamiappan, Review on calcium- and magnesium-based silicates for bone tissue engineering applications, *J. Biomed. Mater. Res., Part A*, 2020, **108**(7), 1546–1562.
14 K. Bavya Devi, S. K. Nandi and M. Roy, Magnesium Silicate Bioceramics for Bone Regeneration: A Review, *J. Indian Inst. Sci.*, 2019, **99**(3), 261–288.
15 S. Ni and J. Chang, In vitro degradation, bioactivity, and cytocompatibility of calcium silicate, dimagnesium silicate, and tricalcium phosphate bioceramics, *J. Biomater. Appl.*, 2009, **24**(2), 139–158.
16 H. Bakhsheshi-Rad, A. Najafinezhad, Z. Hadisi, N. Iqbal, M. Daroonparvar and S. Sharif, *et al.* Characterization and biological properties of nanostructured clinoenstatite scaffolds for bone tissue engineering applications, *Mater. Chem. Phys.*, 2021, **259**, 123969.
17 J.-H. Shin, D.-Y. Lee and S.-H. Lee, Comparison of antimicrobial activity of traditional and new developed root sealers against pathogens related root canal, *J. Dent. Sci.*, 2018, **13**(1), 54–59.
18 P. Singh and A. K. Dubey, Accelerated Osteogenic Response of Electrodynamically Stimulated Mg1–x Ca x Si1–x Zr x O3 (x= 0–0.4) Bioelectrets, *ACS Biomater. Sci. Eng.*, 2023, **9**(11), 6293–6308.
19 B. D. Cullity, *Elements of X-ray, Diffraction*, Addison-Wesley Publishing, 1956.
20 S. M. Londoño-Restrepo, R. Jeronimo-Cruz, B. M. Millán-Malo, E. M. Rivera-Muñoz and M. E. Rodriguez-García, Effect of the nano crystal size on the X-ray diffraction patterns of biogenic hydroxyapatite from human, bovine, and porcine bones, *Sci. Rep.*, 2019, **9**(1), 5915.
21 S. Parthasarathy and V. Parthasarathi, A statistical study on the measurability of Bijvoet differences in crystals with type-I and type-II degree of centrosymmetry, *Acta Crystallogr., Sect. A: Cryst. Phys., Diffr., Theor. Gen. Crystallogr.*, 1976, **32**(5), 768–771.
22 R. D. Shannon, Revised effective ionic radii and systematic studies of interatomic distances in halides and chalcogenides, *Acta Crystallogr., Sect. A*, 1976, **32**(5), 751–767.
23 H. Sun, Q. Zhang, H. Yang and J. Zou, (Ca1− xMgx) SiO3: a low-permittivity microwave dielectric ceramic system, *Mater. Sci. Eng., B*, 2007, **138**(1), 46–50.
24 J. R. Smyth, Experimental study on the polymorphism of enstatite, *Am. Mineral.*, 1974, **59**(3–4), 345–352.
25 C. K. Choi, Comparison between SiOC Thin Film by plasma enhance chemical vapor deposition and SiO2 Thin Film by Fourier Transform Infrared Spectroscopy?, *J. Korean Phys. Soc.*, 2010, **56**(4), 1150–1155.
26 C. Vancea, M. Mihailescu, A. Negrea, G. Mosoarca, M. Ciopec and N. Duteanu, *et al.* Batch and fixed-bed column studies on palladium recovery from acidic solution by modified MgSiO3, *Int. J. Environ. Res. Public Health*, 2020, **17**(24), 9500.
27 S. Sagadevan, S. Venilla, A. Marlinda, M. Johan, Y. A. Wahab and R. Zakaria, *et al.* Effect of synthesis temperature on the morphologies, optical and electrical properties of MgO nanostructures, *J. Nanosci. Nanotechnol.*, 2020, **20**(4), 2488–2494.
28 P. Kumar, B. S. Dehiya, A. Sindhu, R. Kumar, C. I. Pruncu and A. Yadav, Fabrication and characterization of silver nanorods incorporated calcium silicate scaffold using polymeric sponge replica technique, *Mater. Des.*, 2020, **195**, 109026.
29 D. Dufrane, C. Delloye, I. Mckay, P. De Aza, S. De Aza and Y.-J. Schneider, *et al.* Indirect cytotoxicity evaluation of pseudowollastonite, *J. Mater. Sci.: Mater. Med.*, 2003, **14**, 33–38.
30 K. Schwarz, A bound form of silicon in glycosaminoglycans and polyuronides, *Proc. Natl. Acad. Sci. U. S. A.*, 1973, **70**(5), 1608–1612.
31 H. Mohammadi, M. Hafezi, N. Nezafati, S. Heasarki, A. Nadernezhad and S. Ghazanfari, *et al.* Bioinorganics in bioactive calcium silicate ceramics for bone tissue repair: bioactivity and biological properties, *J. Ceram. Sci. Technol.*, 2014, **5**(1), 1–12.
32 P. Pravina, D. Sayaji and M. Avinash, Calcium and its role in human body, *Int. J. Res. Pharm. Biomed. Sci.*, 2013, **4**(2), 659–668.
33 C. Wu, J. Chang, J. Wang, S. Ni and W. Zhai, Preparation and characteristics of a calcium magnesium silicate (bredigite) bioactive ceramic, *Biomaterials*, 2005, **26**(16), 2925–2931.
34 S. Maeno, Y. Niki, H. Matsumoto, H. Morioka, T. Yatabe and A. Funayama, *et al.* The effect of calcium ion concentration on osteoblast viability, proliferation and differentiation in monolayer and 3D culture, *Biomaterials*, 2005, **26**(23), 4847–4855.
35 Y. Ramaswamy, C. Wu, A. Van Hummel, V. Combes, G. Grau and H. Zreiqat, The responses of osteoblasts, osteoclasts and endothelial cells to zirconium modified calcium-silicate-based ceramic, *Biomaterials*, 2008, **29**(33), 4392–4402.
36 J. El Hilaly, Z. H. Israili and B. Lyoussi, Acute and chronic toxicological studies of Ajuga iva in experimental animals, *J. Ethnopharmacol.*, 2004, **91**(1), 43–50.
37 S. A. Bailey, R. H. Zidell and R. W. Perry, Relationships between organ weight and body/brain weight in the rat:

what is the best analytical endpoint?, *Toxicol. Pathol.*, 2004, **32**(4), 448–466.

38 R. Buesen, R. Landsiedel, U. G. Sauer, W. Wohlleben, S. Groeters and V. Strauss, *et al.* Effects of SiO 2, ZrO 2, and BaSO 4 nanomaterials with or without surface functionalization upon 28-day oral exposure to rats, *Arch. Toxicol.*, 2014, **88**, 1881–1906.

39 M. M. Kaplan and A. Righetti, Induction of rat liver alkaline phosphatase: the mechanism of the serum elevation in bile duct obstruction, *J. Clin. Invest.*, 1970, **49**(3), 508–516.

40 Z. Gawlik, E. Fiejka, R. Aleksandrowicz and I. Wiśniewska, Activity of alkaline phosphatase in the healing rat liver after hepatectomy, *Folia Histochem. Cytochem.*, 1978, **16**(4), 343–349.

41 T. M. Wright and A. M. Vandenberg, Risperidone-and quetiapine-induced cholestasis, *Ann. Pharmacother.*, 2007, **41**(9), 1518–1523.

42 A. Singh, T. Bhat and O. Sharma, Clinical biochemistry of hepatotoxicity, *J. Clin. Toxicol.*, 2011, **4**, 1–19.

43 P. N. Kidney, *Textbook of Biochemistry and Human biology*, Prentise Hall India, 1999, pp. 290–296.

44 P. Chan, G. O'hara and A. W. Hayes, Principles and methods for acute and subchronic toxicity, *Principles and methods of toxicology*, 1982, vol. 12, pp. 17–19.

45 O. Adefemi, A. Elujoba and W. Odesanmi, Evaluation of the toxicity potential of Cassia podocarpa with reference to official Senna, *West Afr. J. Pharmacol. Drug Res.*, 1988, **8**, 41–48.

46 R. C. Oh and T. R. Hustead, Causes and evaluation of mildly elevated liver transaminase levels, *Am. Fam. Physician*, 2011, **84**(9), 1003–1008.

47 A. S. Ene-ojo, E. A. Chinedu and F. M. Yakasai, Toxic Effects of Sub-Chronic Administration of Chloroform Extract of Artemisia maciverae Linn on the Kidney of Swiss Albino Rats, 2013.

48 K. L. Timonen, E. Vanninen, J. De Hartog, A. Ibald-Mulli, B. Brunekreef and D. R. Gold, *et al.* Effects of ultrafine and fine particulate and gaseous air pollution on cardiac autonomic control in subjects with coronary artery disease: the ULTRA study, *J. Exposure Sci. Environ. Epidemiol.*, 2006, **16**(4), 332–341.

49 D. Q. Rich, W. Zareba, W. Beckett, P. K. Hopke, D. Oakes and M. W. Frampton, *et al.* Are ambient ultrafine, accumulation mode, and fine particles associated with adverse cardiac responses in patients undergoing cardiac rehabilitation?, *Environ. Health Perspect.*, 2012, **120**(8), 1162–1169.

50 A. Peters, R. Hampel, J. Cyrys, S. Breitner, U. Geruschkat and U. Kraus, *et al.* Elevated particle number concentrations induce immediate changes in heart rate variability: a panel study in individuals with impaired glucose metabolism or diabetes, *Part. Fibre Toxicol.*, 2015, **12**(1), 1–11.

51 R. D. Brook, J. R. Brook, B. Urch, R. Vincent, S. Rajagopalan and F. Silverman, Inhalation of fine particulate air pollution and ozone causes acute arterial vasoconstriction in healthy adults, *Circulation*, 2002, **105**(13), 1534–1536.

52 R. B. Hamanaka and G. M. Mutlu, Particulate matter air pollution: effects on the cardiovascular system, *Front. Endocrinol.*, 2018, **9**, 680.

53 K. E. Ibrahim, M. G. Al-Mutary, A. O. Bakhiet and H. A. Khan, Histopathology of the liver, kidney, and spleen of mice exposed to gold nanoparticles, *Molecules*, 2018, **23**(8), 1848.

54 G. Yan, Y. Huang, Q. Bu, L. Lv, P. Deng and J. Zhou, *et al.* Zinc oxide nanoparticles cause nephrotoxicity and kidney metabolism alterations in rats, *J. Environ. Sci. Health, Part A: Toxic/Hazard. Subst. Environ. Eng.*, 2012, **47**(4), 577–588.

55 A. Noori, F. Karimi, S. Fatahian and F. Yazdani, Effects of zinc oxide nanoparticles on renal function in mice, *Int. J. Biosci.*, 2014, **5**(9), 140–146.

56 J. Lipka, M. Semmler-Behnke, R. A. Sperling, A. Wenk, S. Takenaka and C. Schleh, *et al.* Biodistribution of PEG-modified gold nanoparticles following intratracheal instillation and intravenous injection, *Biomaterials*, 2010, **31**(25), 6574–6581.

57 M. Husain, D. Wu, A. T. Saber, N. Decan, N. R. Jacobsen and A. Williams, *et al.* Intratracheally instilled titanium dioxide nanoparticles translocate to heart and liver and activate complement cascade in the heart of C57BL/6 mice, *Nanotoxicology*, 2015, **9**(8), 1013–1022.

58 J. Modrzynska, A. Mortensen, T. Berthing, G. Ravn-Haren, J. Szarek and A. T. Saber, *et al.* Effect on mouse liver morphology of CeO2, TiO2 and carbon black nanoparticles translocated from lungs or deposited intravenously, *Appl. Nanosci.*, 2021, **2**(3), 222–241.

59 M. A. K. Abdelhalim and B. M. Jarrar, Gold nanoparticles administration induced prominent inflammatory, central vein intima disruption, fatty change and Kupffer cells hyperplasia, *Lipids Health Dis.*, 2011, **10**, 1–6.

60 M. A. K. Abdelhalim and B. M. Jarrar, Gold nanoparticles induced cloudy swelling to hydropic degeneration, cytoplasmic hyaline vacuolation, polymorphism, binucleation, karyopyknosis, karyolysis, karyorrhexis and necrosis in the liver, *Lipids Health Dis.*, 2011, **10**, 1–6.

61 M. A. K. Abdelhalim, Gold nanoparticles administration induces disarray of heart muscle, hemorrhagic, chronic inflammatory cells infiltrated by small lymphocytes, cytoplasmic vacuolization and congested and dilated blood vessels, *Lipids Health Dis.*, 2011, **10**(1), 1–9.

62 Z. Sheikh, P. J. Brooks, O. Barzilay, N. Fine and M. Glogauer, Macrophages, foreign body giant cells and their response to implantable biomaterials, *Materials*, 2015, **8**(9), 5671–5701.

63 Z. Xia and J. T. Triffitt, A review on macrophage responses to biomaterials, *Biomed. Mater.*, 2006, **1**(1), R1.

64 A. Sergijenko, A. J. Roelofs, A. H. Riemen and C. De Bari, Bone marrow contribution to synovial hyperplasia following joint surface injury, *Arthritis Res. Ther.*, 2016, **18**, 1–11.

65 Synovial cellular and molecular markers in rheumatoid arthritis, *Seminars in immunopathology*, ed. M. Asif Amin, D. A. Fox and J. H. Ruth, Springer, 2017.

66 C. J. Burke, H. Alizai, L. S. Beltran and R. R. Regatte, MRI of synovitis and joint fluid, *J. Magn. Reson. Imaging*, 2019, **49**(6), 1512–1527.
67 S. Lerouge, O. Huk, L. H. Yahia and L. Sedel, Characterization of in vivo wear debris from ceramic—ceramic total hip arthroplasties, *J. Biomed. Mater. Res.*, 1996, **32**(4), 627–633.
68 A. Hatton, J. Nevelos, A. Nevelos, R. Banks, J. Fisher and E. Ingham, Alumina–alumina artificial hip joints. Part I: a histological analysis and characterisation of wear debris by laser capture microdissection of tissues retrieved at revision, *Biomaterials*, 2002, **23**(16), 3429–3440.
69 S.-Y. Yang, W. Ren, Y. Park, A. Sieving, S. Hsu and S. Nasser, *et al.* Diverse cellular and apoptotic responses to variant shapes of UHMWPE particles in a murine model of inflammation, *Biomaterials*, 2002, **23**(17), 3535–3543.
70 G. Thrivikraman, G. Madras and B. Basu, In vitro/in vivo assessment and mechanisms of toxicity of bioceramic materials and its wear particulates, *RSC Adv.*, 2014, **4**(25), 12763–12781.